Title
Ewald method for 3D periodic dyadic Green's functions and complex modes in composite materials made of spherical particles under the dual dipole approximation

Journal
Radio Science, 47(4)

ISSN
0048-6604

Authors
Campione, S
Capolino, F

Publication Date
2012-10-12

DOI
10.1029/2012RS005031

Ewald method for 3D periodic dyadic Green's functions and complex modes in composite materials made of spherical particles under the dual dipole approximation

Salvatore Campione[1] and Filippo Capolino[1]

Received 2 April 2012; revised 9 July 2012; accepted 19 July 2012; published 26 September 2012.

[1] We derive the Ewald representation for the dyadic periodic Green's functions to represent the electromagnetic field in a three dimensional (3D) periodic array of electric and magnetic dipoles. Then we use the developed theory to analyze the modes with real and complex wave number in a 3D periodic lattice of lead telluride (PbTe) microspheres at infrared frequencies and in a 3D periodic lattice of titanium dioxide (TiO_2) microspheres at millimeter waves. Each microsphere is equivalently modeled with both an electric and a magnetic dipole, via a method here called the dual dipole approximation (DDA). The 3D lattices exhibit first a magnetic-induced then an electric-induced feature determined by microsphere magnetic and electric resonances. The DDA wave number results are compared to the ones computed with single electric or single magnetic dipole approximation and to the ones retrieved by using the Nicolson-Ross-Weir (NRW) retrieval method from reflection and transmission of finite thickness slabs computed by a full-wave simulation. It is shown that the DDA method is in very good agreement with NRW, in contrast to the previously reported single dipole approximation methods that fail to predict one of the two features (either electric or magnetic). A mode with transverse polarization is found to be dominant and able to propagate inside the lattice, and therefore the composite material can be treated as a homogeneous one with effective refractive index. This is obtained by adopting five different retrieval procedures for each lattice, and their agreement or disagreement is discussed.

Citation: Campione, S., and F. Capolino (2012), Ewald method for 3D periodic dyadic Green's functions and complex modes in composite materials made of spherical particles under the dual dipole approximation, *Radio Sci.*, *47*, RS0N06, doi:10.1029/2012RS005031.

1. Introduction

[2] Artificial composite materials (metamaterials) proved to be a feasible way to increase the degrees of freedom in the interaction of electromagnetic fields with matter from microwaves to optical frequencies.

[3] Collective resonances and wave propagation in composite materials can be characterized by modal analyses of arrays periodic in three dimensions (3D) [*Alù and Engheta*, 2007; *Benenson*, 1971; *Campione et al.*, 2011a, 2011b, 2012; *Ham and Segall*, 1961; *Shore and Yaghjian*, 2007, 2010, 2012; *Steshenko and Capolino*, 2009; *Wheeler et al.*, 2005b]. In particular, under certain circumstances of polarization and excitation, a 3D periodic array of particles with finite thickness could be described with good approximation as a homogeneous slab with effective parameters [*Campione et al.*, 2011a, 2011b, 2012; *Collin*, 1960; *Shore and Yaghjian*, 2012], such as relative permittivity (ε_{eff}), relative permeability (μ_{eff}), and refractive index (n_{eff}).

[4] The aim of this paper is to characterize the modes with real and complex wave number in 3D periodic arrays made of particles with spherical shape modeled through the dual (electric and magnetic) dipole approximation (DDA). The DDA is a good approximation when the two dipolar terms (or any of them) dominate the scattered-field multipole expansion. For transverse polarization, the structure is treated as a homogeneous slab with effective refractive index. Here we are interested in analyzing composite materials made of large dielectric permittivity materials (e.g., lead telluride, titanium dioxide, etc.) which in general exhibit first a magnetic then an electric resonance. The DDA is more accurate than the single dipole approximation (SDA) approach, since it accounts for electric and magnetic couplings, and the method described here could also be used to characterize the artificial magnetic (i.e., $\mu_{\text{eff}} \neq 1$) or electric (i.e., $\varepsilon_{\text{eff}} \neq 1$) properties of the 3D lattice. Possible routes for obtaining artificial magnetism,

[1]Department of Electrical Engineering and Computer Science, University of California, Irvine, California, USA.

Corresponding author: F. Capolino, Department of Electrical Engineering and Computer Science, University of California, 4131 Engineering Hall, Irvine, CA 92697, USA. (f.capolino@uci.edu)

0048-6604/12/2012RS005031

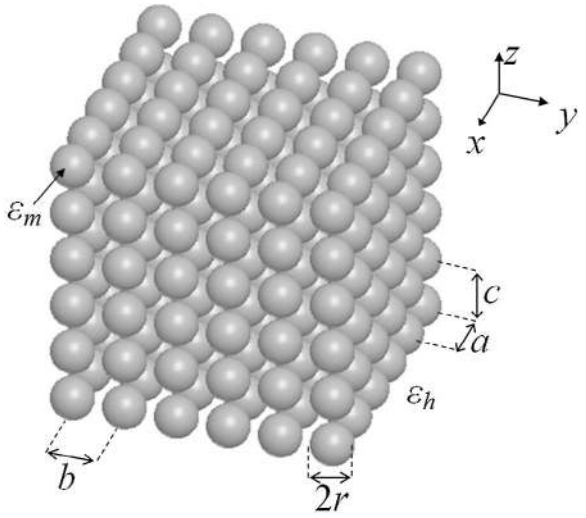

Figure 1. Three-dimensional periodic array made of spherical particles with relative permittivity ε_m embedded in a homogeneous medium with relative permittivity ε_h. The radius of each sphere is denoted as r and a, b and c are the periodicities along the x-, y- and z-directions, respectively.

such as the use of split ring resonators, binary mixtures, etc., have been recently summarized in the introduction of *Campione et al.* [2012]. The present work has been indeed partly motivated by the observations made in [*Campione et al.*, 2012] about the fact that the results shown in that paper could be further improved by modeling the particle with the DDA model, instead of the two SDA models based only on magnetic dipoles shown therein.

[5] The approach described in the present paper allows for the tracking and especially for the characterization of the evolution of modes varying frequency. First, we develop the formulation with coupled electric and magnetic dipoles through DDA to model the particle behavior (as done, for example, in *Mulholland et al.* [1994] and *Shore and Yaghjian* [2010, 2012]) in order to analyze modes with real and complex wave number in 3D periodic arrays of spherical particles. The numerical procedure developed in this paper for evaluating the complex zeros of the dispersion relation uses the Ewald representation for the *dyadic* periodic Green's functions (GFs) to represent the field in 3D periodic arrays, and is partly based on previous scalar developments [*Kustepeli and Martin*, 2000; *Lovat et al.*, 2008; *Park et al.*, 1998; *Stevanoviæ and Mosig*, 2007] and dyadic developments [*Campione et al.*, 2011b, 2012]. The Ewald representation, besides providing analytic continuation to the complex wave number space, results in two series with Gaussian convergence where only a handful of terms are needed [*Ewald*, 1921; *Kustepeli and Martin*, 2000; *Lovat et al.*, 2008; *Park et al.*, 1998; *Stevanoviæ and Mosig*, 2007]. In *Shore and Yaghjian* [2010, 2012] the authors treat similar problems of arrays of spherical particles where both electric and magnetic dipoles have been considered. They evaluate the modes with complex wave number by using a method based on polylogarithmic functions, which is different from the Ewald method employed here. Furthermore, in our formulation, the direction of electric and magnetic dipoles is arbitrary.

[6] The structure of the paper is as follows. We discuss in section 2 the rigorous representation of the field in 3D periodic arrays using the dyadic GFs including the case with coupled electric and magnetic dipoles. Then, in section 3, we derive the new expressions for the dyadic GFs using the Ewald method related to both electric and magnetic dipole excitations. The convergence properties of scalar and dyadic GFs are briefly inspected as well. Last, in section 4, we analyze the modal wave numbers for transverse polarization in two composite metamaterials: one made of an array of non-magnetic lead telluride (PbTe) microspheres, and the other made of non-magnetic titanium dioxide (TiO_2) microspheres. Modal wave numbers are computed through various methods: DDA, SDA based on electric dipoles only (SDA-E), SDA based on magnetic dipoles only (SDA-M), and Nicolson-Ross-Weir (NRW) retrieval method from reflection and transmission of finite thickness slabs computed by full-wave simulations. The 3D lattices are then described in terms of effective refractive index, computed by using the four methods above and Maxwell Garnett (MG) formulas, and their agreement or disagreement is discussed. The procedure for the singularity regularization of the spatial series counterparts in the Ewald representations is discussed in Appendix A. Supporting mathematical expressions are reported in Appendix B.

2. Formulation Using Periodic Green's Functions

[7] The monochromatic time harmonic convention $\exp(-i\omega t)$ is assumed here and throughout the paper, and is therefore suppressed hereafter. In the following equations, bold letters refer to vector quantities, a caret '^' on top of a bold letter refers to unit vectors, and a bar under a bold letter refers to dyadic quantities.

2.1. Field in Periodic Arrays

[8] Consider a 3D periodic array of particles (Figure 1) described by dipole-like electric and magnetic polarizabilities. Each particle is characterized by its induced electric (**p**) and magnetic (**m**) dipole moments as described in section 2.4. The array is immersed in a homogeneous background, with relative permittivity ε_h. Particles are placed at positions $\mathbf{r}_n = \mathbf{r}_0 + \mathbf{d}_n$, where $\mathbf{d}_n = n_1 a\hat{\mathbf{x}} + n_2 b\hat{\mathbf{y}} + n_3 c\hat{\mathbf{z}}$, $n = (n_1, n_2, n_3)$ is a triple index with $n_1, n_2, n_3 = 0, \pm 1, \pm 2, \ldots$, $\mathbf{r}_0 = x_0\hat{\mathbf{x}} + y_0\hat{\mathbf{y}} + z_0\hat{\mathbf{z}}$ denotes a reference particle location, and a, b and c are the periodicities along the x-, y- and z-directions, respectively [*Campione et al.*, 2011b, 2012; *Steshenko and Capolino*, 2009].

[9] Suppose that the 3D array is either excited by an external incident field or supports a mode, with wave vector $\mathbf{k}_B = k_x\hat{\mathbf{x}} + k_y\hat{\mathbf{y}} + k_z\hat{\mathbf{z}}$, such that the nth dipole (at $\mathbf{r}_n$) is related to the 0th one (at $\mathbf{r}_0$) by $\mathbf{p}_n = \mathbf{p}_0 \exp(i\mathbf{k}_B \cdot \mathbf{d}_n)$ and $\mathbf{m}_n = \mathbf{m}_0 \exp(i\mathbf{k}_B \cdot \mathbf{d}_n)$. Then, the electric and magnetic fields at a general position **r** are given by

$$\begin{bmatrix} \mathbf{E}(\mathbf{r}) \\ \mathbf{H}(\mathbf{r}) \end{bmatrix} = \begin{bmatrix} \mathbf{E}^{\mathrm{inc}}(\mathbf{r}) \\ \mathbf{H}^{\mathrm{inc}}(\mathbf{r}) \end{bmatrix} + \begin{bmatrix} \underline{\mathbf{G}}^{\infty}_{\mathrm{EP}}(\mathbf{r}, \mathbf{r}_0, \mathbf{k}_B) & \underline{\mathbf{G}}^{\infty}_{\mathrm{EM}}(\mathbf{r}, \mathbf{r}_0, \mathbf{k}_B) \\ \underline{\mathbf{G}}^{\infty}_{\mathrm{HP}}(\mathbf{r}, \mathbf{r}_0, \mathbf{k}_B) & \underline{\mathbf{G}}^{\infty}_{\mathrm{HM}}(\mathbf{r}, \mathbf{r}_0, \mathbf{k}_B) \end{bmatrix} \cdot \begin{bmatrix} \mathbf{p}_0 \\ \mathbf{m}_0 \end{bmatrix}. \tag{1}$$

[10] The Green's function matrix in (1) accounts for all the coupling between electric and magnetic dipoles. The blocks $\underline{\mathbf{G}}^{\infty}_{\mathrm{EP}}$ and $\underline{\mathbf{G}}^{\infty}_{\mathrm{HM}}$ in the principal diagonal of (1) represent the

periodic Green's functions that connect all $\mathbf{p}_n$ to $\mathbf{E}$ and all $\mathbf{m}_n$ to $\mathbf{H}$, respectively. The blocks in the antidiagonal $\underline{\mathbf{G}}^{\infty}_{\mathrm{EM}}$ and $\underline{\mathbf{G}}^{\infty}_{\mathrm{HP}}$ represent the periodic Green's functions that connect all $\mathbf{m}_n$ to $\mathbf{E}$ and all $\mathbf{p}_n$ to $\mathbf{H}$, respectively.

2.2. Principal Diagonal Blocks: $\underline{\mathbf{G}}^{\infty}_{\mathbf{EP}}$ and $\underline{\mathbf{G}}^{\infty}_{\mathbf{HM}}$

[11] Both the principal diagonal blocks $\underline{\mathbf{G}}^{\infty}_{\mathrm{EP}}(\mathbf{r}, \mathbf{r}_0, \mathbf{k}_{\mathrm{B}}) = (\varepsilon_0\varepsilon_h)^{-1}\underline{\mathbf{G}}^{\infty}_{\mathrm{pd}}(\mathbf{r}, \mathbf{r}_0, \mathbf{k}_{\mathrm{B}})$ [*Campione et al.*, 2011b] and $\underline{\mathbf{G}}^{\infty}_{\mathrm{HM}}(\mathbf{r}, \mathbf{r}_0, \mathbf{k}_{\mathrm{B}}) = \underline{\mathbf{G}}^{\infty}_{\mathrm{pd}}(\mathbf{r}, \mathbf{r}_0, \mathbf{k}_{\mathrm{B}})$ [*Campione et al.*, 2012] are defined in terms of a "principal diagonal" dyad $\underline{\mathbf{G}}^{\infty}_{\mathrm{pd}}$ for the periodically phased array of dipoles, defined as

$$\underline{\mathbf{G}}^{\infty}_{\mathrm{pd}}(\mathbf{r}, \mathbf{r}_0, \mathbf{k}_{\mathrm{B}}) = \sum_{n=-\infty}^{+\infty} \underline{\mathbf{G}}_{\mathrm{pd}}(\mathbf{r}, \mathbf{r}_n)\, e^{i\mathbf{k}_{\mathrm{B}}\cdot\mathbf{d}_n}. \tag{2}$$

[12] Here $\underline{\mathbf{G}}_{\mathrm{pd}}(\mathbf{r}, \mathbf{r}_0)$ denotes the "free space" dyadic Green's function in the homogeneous background, given by *Campione et al.* [2012, equation (6)]. The principal diagonal dyad $\underline{\mathbf{G}}^{\infty}_{\mathrm{pd}}$ can be also expressed as

$$\underline{\mathbf{G}}^{\infty}_{\mathrm{pd}}(\mathbf{r}, \mathbf{r}_0, \mathbf{k}_{\mathrm{B}}) = k^2 G^{\infty}(\mathbf{r}, \mathbf{r}_0, \mathbf{k}_{\mathrm{B}})\, \underline{\mathbf{I}} + \nabla\nabla G^{\infty}(\mathbf{r}, \mathbf{r}_0, \mathbf{k}_{\mathrm{B}}), \tag{3}$$

which will be used later in section 3.1, where the scalar term G^{∞} is represented as a sum of "spatial" spherical waves as

$$G^{\infty}(\mathbf{r}, \mathbf{r}_0, \mathbf{k}_{\mathrm{B}}) = \sum_{n=-\infty}^{+\infty} G(\mathbf{r}, \mathbf{r}_n)\, e^{i\mathbf{k}_{\mathrm{B}}\cdot\mathbf{d}_n}, \tag{4}$$

where $G(\mathbf{r}, \mathbf{r}_0) = e^{ikR}/(4\pi R)$, with $R = |\mathbf{R}|$ and $\mathbf{R} = \mathbf{r} - \mathbf{r}_0$. Moreover, $k = \omega\sqrt{\varepsilon_h}/c_0 = k_0\sqrt{\varepsilon_h}$ is the host wave number, where k_0 denotes the free space wave number and c_0 the speed of light in free space, ε_h is the relative permittivity of the host medium, and $\underline{\mathbf{I}}$ is the unit dyad.

2.3. Antidiagonal Blocks: $\underline{\mathbf{G}}^{\infty}_{\mathbf{EM}}$ and $\underline{\mathbf{G}}^{\infty}_{\mathbf{HP}}$

[13] Both antidiagonal blocks $\underline{\mathbf{G}}^{\infty}_{\mathrm{EM}}(\mathbf{r}, \mathbf{r}_0, \mathbf{k}_{\mathrm{B}}) = i\mu\omega\underline{\mathbf{G}}^{\infty}_{\mathrm{ad}}(\mathbf{r}, \mathbf{r}_0, \mathbf{k}_{\mathrm{B}})$ and $\underline{\mathbf{G}}^{\infty}_{\mathrm{HP}}(\mathbf{r}, \mathbf{r}_0, \mathbf{k}_{\mathrm{B}}) = -i\omega\underline{\mathbf{G}}^{\infty}_{\mathrm{ad}}(\mathbf{r}, \mathbf{r}_0, \mathbf{k}_{\mathrm{B}})$ are defined in terms of an "antidiagonal" dyad $\underline{\mathbf{G}}^{\infty}_{\mathrm{ad}}$ for the periodic phased array of dipoles, computed as

$$\underline{\mathbf{G}}^{\infty}_{\mathrm{ad}}(\mathbf{r}, \mathbf{r}_0, \mathbf{k}_{\mathrm{B}}) = \sum_{n=-\infty}^{+\infty} \underline{\mathbf{G}}_{\mathrm{ad}}(\mathbf{r}, \mathbf{r}_n)\, e^{i\mathbf{k}_{\mathrm{B}}\cdot\mathbf{d}_n}. \tag{5}$$

[14] Here $\underline{\mathbf{G}}_{\mathrm{ad}}(\mathbf{r}, \mathbf{r}_0)$ denotes the "free space" dyadic Green's function in the homogeneous background, defined as $\underline{\mathbf{G}}_{\mathrm{ad}}(\mathbf{r}, \mathbf{r}_0) = \nabla G(\mathbf{r}, \mathbf{r}_0) \times \underline{\mathbf{I}}$, and hence

$$\underline{\mathbf{G}}_{\mathrm{ad}}(\mathbf{r}, \mathbf{r}_0) = \frac{ik}{4\pi}\frac{e^{ikR}}{R}\left(1 - \frac{1}{ikR}\right)\left(\hat{\mathbf{R}} \times \underline{\mathbf{I}}\right), \tag{6}$$

where $\mathbf{R} = \mathbf{r} - \mathbf{r}_0$, $R = |\mathbf{R}|$ and $\hat{\mathbf{R}} = \mathbf{R}/R$. The antidiagonal dyad $\underline{\mathbf{G}}^{\infty}_{\mathrm{ad}}$ for the 3D periodic array can be also expressed as

$$\underline{\mathbf{G}}^{\infty}_{\mathrm{ad}}(\mathbf{r}, \mathbf{r}_0, \mathbf{k}_{\mathrm{B}}) = \nabla G^{\infty}(\mathbf{r}, \mathbf{r}_0, \mathbf{k}_{\mathrm{B}}) \times \underline{\mathbf{I}}, \tag{7}$$

with $G^{\infty}(\mathbf{r}, \mathbf{r}_0, \mathbf{k}_{\mathrm{B}})$ the scalar GF in (4), and this will be used later in section 3.2.

2.4. Spherical Particle Modeling and Modal Analysis in 3D Arrays

[15] The induced electric ($\mathbf{p}_0$) and magnetic ($\mathbf{m}_0$) dipole moments for the 0th spherical particle at position $\mathbf{r}_0$ are given by [*Alù and Engheta*, 2006; *Ishimaru et al.*, 2003]

$$\begin{bmatrix} \mathbf{p}_0 \\ \mathbf{m}_0 \end{bmatrix} = \underbrace{\begin{bmatrix} \underline{\boldsymbol{\alpha}}_{\mathrm{ee}} & \underline{\boldsymbol{\alpha}}_{\mathrm{em}} \\ \underline{\boldsymbol{\alpha}}_{\mathrm{me}} & \underline{\boldsymbol{\alpha}}_{\mathrm{mm}} \end{bmatrix}}_{\underline{\underline{\boldsymbol{\alpha}}}} \begin{bmatrix} \mathbf{E}^{\mathrm{loc}}(\mathbf{r}_0) \\ \mathbf{H}^{\mathrm{loc}}(\mathbf{r}_0) \end{bmatrix} \tag{8}$$

where $\underline{\underline{\boldsymbol{\alpha}}}$ is a 6×6 matrix, $\underline{\boldsymbol{\alpha}}_{\mathrm{ee}} = \alpha_{\mathrm{ee}}\underline{\mathbf{I}}$ and $\underline{\boldsymbol{\alpha}}_{\mathrm{mm}} = \alpha_{\mathrm{mm}}\underline{\mathbf{I}}$, with α_{ee} and α_{mm} the isotropic electric and magnetic polarizabilities of the spherical particle. Moreover, here we assume $\underline{\boldsymbol{\alpha}}_{\mathrm{em}} = \underline{\boldsymbol{\alpha}}_{\mathrm{me}} = \underline{\mathbf{0}}$ in the dipole approximation [*Alù and Engheta*, 2006], with $\underline{\mathbf{0}}$ being the null dyad. Therefore in this paper we are limiting the nanoparticle interactions to only the dipole-dipole terms, however including both electric and magnetic ones, and this approximation is very satisfactory for a large class of problems involving collections of nanoparticles or microparticles [*Capolino*, 2009].

[16] According to Mie theory, the electric and magnetic polarizabilities of a sphere are [*Bohren and Huffman*, 1983; *Steshenko and Capolino*, 2009; *Wheeler et al.*, 2005a]

$$\alpha_{\mathrm{ee}} = \frac{6\pi i\varepsilon_0\varepsilon_h}{k^3}a_1, \quad \alpha_{\mathrm{mm}} = \frac{6\pi i}{k^3}b_1 \tag{9}$$

with

$$a_1 = \frac{m_r\psi_1(m_r kr)\psi_1'(kr) - \psi_1(kr)\psi_1'(m_r kr)}{m_r\psi_1(m_r kr)\xi_1'(kr) - \xi_1(kr)\psi_1'(m_r kr)}, \tag{10}$$

$$b_1 = \frac{\psi_1(m_r kr)\psi_1'(kr) - m_r\psi_1(kr)\psi_1'(m_r kr)}{\psi_1(m_r kr)\xi_1'(kr) - m_r\xi_1(kr)\psi_1'(m_r kr)}. \tag{11}$$

[17] In (9)–(11), r is the sphere radius, a_1 and b_1 are the electric and magnetic Mie dipole scattering coefficients [*Bohren and Huffman*, 1983], respectively, $\psi_1(\rho) = \rho j_1(\rho) = \sin\rho/\rho - \cos\rho$ and $\xi_1(\rho) = \rho h_1^{(1)}(\rho) = (-i/\rho - 1)e^{i\rho}$ are the Riccati-Bessel functions [*Abramowitz and Stegun*, 1965], $m_r = \sqrt{\varepsilon_m/\varepsilon_h}$ is the relative refractive index contrast, and ε_m is the relative permittivity of the spheres. Notice that a prime in (10) and (11) refers to the first derivative of the functions $\psi_1(\rho)$ and $\xi_1(\rho)$ with respect to their argument ρ.

[18] The local fields $\mathbf{E}^{\mathrm{loc}}$ and $\mathbf{H}^{\mathrm{loc}}$ in (8) acting on the 0th particle at position $\mathbf{r}_0$ are computed as [*Campione et al.*, 2011b, 2012; *Steshenko and Capolino*, 2009]

$$\begin{bmatrix} \mathbf{E}^{\mathrm{loc}}(\mathbf{r}_0) \\ \mathbf{H}^{\mathrm{loc}}(\mathbf{r}_0) \end{bmatrix} = \underbrace{\begin{bmatrix} \breve{\underline{\mathbf{G}}}^{\infty}_{\mathrm{EP}}(\mathbf{r}_0, \mathbf{r}_0, \mathbf{k}_{\mathrm{B}}) & \breve{\underline{\mathbf{G}}}^{\infty}_{\mathrm{EM}}(\mathbf{r}_0, \mathbf{r}_0, \mathbf{k}_{\mathrm{B}}) \\ \breve{\underline{\mathbf{G}}}^{\infty}_{\mathrm{HP}}(\mathbf{r}_0, \mathbf{r}_0, \mathbf{k}_{\mathrm{B}}) & \breve{\underline{\mathbf{G}}}^{\infty}_{\mathrm{HM}}(\mathbf{r}_0, \mathbf{r}_0, \mathbf{k}_{\mathrm{B}}) \end{bmatrix}}_{\underline{\underline{\mathbf{A}}}(\mathbf{k}_{\mathrm{B}})} \cdot \begin{bmatrix} \mathbf{p}_0 \\ \mathbf{m}_0 \end{bmatrix}, \tag{12}$$

where $\underline{\underline{\mathbf{A}}}$ is a 6×6 matrix, since each block is a 3×3 matrix. In the definition of the local fields in (12) the contribution from the 0th particle itself has been removed and

the value of the regularized periodic GF $\breve{\underline{\mathbf{G}}}^{\infty}(\mathbf{r}_0, \mathbf{r}_0, \mathbf{k}_B)$ (either in the principal or antidiagonal) is determined by the limit $\breve{\underline{\mathbf{G}}}^{\infty}(\mathbf{r}_0, \mathbf{r}_0, \mathbf{k}_B) = \lim_{\mathbf{r}\to\mathbf{r}_0}[\underline{\mathbf{G}}^{\infty}(\mathbf{r}, \mathbf{r}_0, \mathbf{k}_B) - \underline{\mathbf{G}}(\mathbf{r}, \mathbf{r}_0)]$ since both $\underline{\mathbf{G}}^{\infty}$ and $\underline{\mathbf{G}}$ are singular at $\mathbf{r} = \mathbf{r}_0$. In particular, the principal diagonal GFs possess a singularity at the source location which is of one higher power in $|\mathbf{r} - \mathbf{r}_0|$ than the antidiagonal ones, as also stated in *Yaghjian* [1980].

[19] By combining (12) with (8), one obtains a linear system from which one could compute the modal complex wave numbers by solving

$$\det\left[\underline{\underline{\boldsymbol{\alpha}}}^{-1} - \underline{\underline{\mathbf{A}}}(\mathbf{k}_B)\right] = 0 \tag{13}$$

for complex $\mathbf{k}_B$.

3. Ewald Representation for the Dyadic GFs for 3D Periodic Arrays

3.1. Expressions for the Regularized Principal Diagonal Dyad $\breve{\underline{\mathbf{G}}}^{\infty}_{\mathbf{pd}}$

[20] According to the Ewald representation [*Ewald*, 1921; *Ham and Segall*, 1961] the scalar GF in (4) for a 3D array of dipoles is split into the hybrid sum of spectral and spatial scalar terms

$$G^{\infty}(\mathbf{r}, \mathbf{r}_0, \mathbf{k}_B) = G^{\infty}_{\text{spectral}}(\mathbf{r}, \mathbf{r}_0, \mathbf{k}_B) + G^{\infty}_{\text{spatial}}(\mathbf{r}, \mathbf{r}_0, \mathbf{k}_B), \tag{14}$$

as described also in *Kustepeli and Martin* [2000], *Lovat et al.* [2008], *Park et al.* [1998], and *Stevanoviæ and Mosig* [2007]. Accordingly,

$$G^{\infty}_{\text{spectral}}(\mathbf{r}, \mathbf{r}_0, \mathbf{k}_B) = \frac{1}{abc}\sum_{n=-\infty}^{+\infty}\frac{e^{-\frac{\gamma_n^2}{4E^2}}}{\gamma_n^2}e^{i(\mathbf{k}_B+\mathbf{k}_n)\cdot(\mathbf{r}-\mathbf{r}_0)} \tag{15}$$

$$G^{\infty}_{\text{spatial}}(\mathbf{r}, \mathbf{r}_0, \mathbf{k}_B) = \frac{1}{8\pi}\sum_{n=-\infty}^{+\infty}\frac{e^{i\mathbf{k}_B\cdot\mathbf{d}_n}}{R_n}f(R_n) \tag{16}$$

where $\gamma_n^2 = |\mathbf{k}_B + \mathbf{k}_n|^2 - k^2$, with $\mathbf{k}_n = (2\pi n_1/a)\hat{\mathbf{x}} + (2\pi n_2/b)\hat{\mathbf{y}} + (2\pi n_3/c)\hat{\mathbf{z}}$, and

$$f(R_n) = e^{-ikR_n}\text{erfc}(\beta^-) + e^{+ikR_n}\text{erfc}(\beta^+). \tag{17}$$

[21] The function erfc(ν) denotes the complementary error function [*Abramowitz and Stegun*, 1965] of argument $\beta^{\pm} = R_nE \pm ik/(2E)$. The adopted Ewald parameter E is [*Kustepeli and Martin*, 2000]

$$E = \left[\pi^2\frac{1/a^2 + 1/b^2 + 1/c^2}{a^2 + b^2 + c^2}\right]^{1/4} \tag{18}$$

which is chosen based on optimizing the total number of necessary terms in both the scalar spatial and spectral series, since with this choice they both exhibit the same Gaussian convergence rate. Note that the spatial $1/R$ singularity is fully represented by the $n = 0$ term of the spatial sum.

[22] Similarly to what discussed after (12), the regularized scalar periodic GF evaluated at $\mathbf{r}_0$ is given by $\breve{G}^{\infty}_{\text{spatial}}(\mathbf{r}_0, \mathbf{r}_0, \mathbf{k}_B) = \lim_{\mathbf{r}\to\mathbf{r}_0}[G^{\infty}_{\text{spatial}}(\mathbf{r}, \mathbf{r}_0, \mathbf{k}_B) - G(\mathbf{r}, \mathbf{r}_0)]$. After performing the limit for $\mathbf{r} \to \mathbf{r}_0$ (see details in the Appendix A) one has

$$\breve{G}^{\infty}_{\text{spatial}}(\mathbf{r}_0, \mathbf{r}_0, \mathbf{k}_B) = \frac{1}{8\pi}\sum_{n\neq(0,0,0)}\frac{e^{i\mathbf{k}_B\cdot\mathbf{d}_n}}{R_n}f(R_n) + \frac{f'(0) - 2ik}{8\pi}. \tag{19}$$

[23] In (19) a prime (f') denotes a derivative of f in (17) with respect to its argument R_n, whose expression is given in Appendix B.

[24] Then, we accordingly split the dyadic GF in (3) as

$$\underline{\mathbf{G}}^{\infty}_{\text{pd}}(\mathbf{r}, \mathbf{r}_0, \mathbf{k}_B) = \underline{\mathbf{G}}^{\infty}_{\text{pd,spectral}}(\mathbf{r}, \mathbf{r}_0, \mathbf{k}_B) + \underline{\mathbf{G}}^{\infty}_{\text{pd,spatial}}(\mathbf{r}, \mathbf{r}_0, \mathbf{k}_B), \tag{20}$$

where

$$\underline{\mathbf{G}}^{\infty}_{\text{pd,type}}(\mathbf{r}, \mathbf{r}_0, \mathbf{k}_B) = k^2G^{\infty}_{\text{type}}(\mathbf{r}, \mathbf{r}_0, \mathbf{k}_B)\underline{\mathbf{I}} + \nabla\nabla G^{\infty}_{\text{type}}(\mathbf{r}, \mathbf{r}_0, \mathbf{k}_B), \tag{21}$$

where "type" is either spectral or spatial. The first term of the dyad in (21) is proportional to the scalar GF which is given in (15) for the spectral and in (16) for the spatial type. The terms $\nabla\nabla G^{\infty}_{\text{spectral}}$ and $\nabla\nabla G^{\infty}_{\text{spatial}}$ are derived based on (15) and (16) leading to

$$\nabla\nabla G^{\infty}_{\text{spectral}}(\mathbf{r}, \mathbf{r}_0, \mathbf{k}_B) = -\frac{1}{abc}\sum_{n=-\infty}^{+\infty}(\mathbf{k}_B + \mathbf{k}_n)(\mathbf{k}_B + \mathbf{k}_n)\frac{e^{-\frac{\gamma_n^2}{4E^2}}}{\gamma_n^2} \cdot e^{i(\mathbf{k}_B+\mathbf{k}_n)\cdot(\mathbf{r}-\mathbf{r}_0)}, \tag{22}$$

and

$$\nabla\nabla G^{\infty}_{\text{spatial}}(\mathbf{r}, \mathbf{r}_0, \mathbf{k}_B) = \frac{1}{8\pi}\sum_{n=-\infty}^{+\infty}e^{i\mathbf{k}_B\cdot\mathbf{d}_n}\underline{\mathbf{F}}_{\text{spatial},n}, \tag{23}$$

where

$$\underline{\mathbf{F}}_{\text{spatial},n} = \left(\frac{f'(R_n)}{R_n^2} - \frac{f(R_n)}{R_n^3}\right)\underline{\mathbf{I}} + \left(\frac{f''(R_n)}{R_n} - \frac{3f'(R_n)}{R_n^2} + \frac{3f(R_n)}{R_n^3}\right)\hat{\mathbf{R}}_n\hat{\mathbf{R}}_n, \tag{24}$$

and $\hat{\mathbf{R}}_n = \mathbf{R}_n/R_n$. Furthermore, f'' and f''' are the second and third derivatives of f in (17) with respect to its argument R_n, respectively, whose expressions are given in Appendix B. Similarly to what discussed for the scalar GF, here $\nabla\nabla\breve{G}^{\infty}_{\text{spatial}}(\mathbf{r}_0, \mathbf{r}_0, \mathbf{k}_B) = \lim_{\mathbf{r}\to\mathbf{r}_0}[\nabla\nabla G^{\infty}_{\text{spatial}}(\mathbf{r}, \mathbf{r}_0, \mathbf{k}_B) - \nabla\nabla G(\mathbf{r}, \mathbf{r}_0)]$. In its computation we need to evaluate the limit because both $\nabla\nabla G^{\infty}_{\text{spatial}}$ and $\nabla\nabla G$ have singular terms at $\mathbf{r} = \mathbf{r}_0$ of the kind $1/R_0^p$ with $p = 1, 2, 3$. After performing the limit for $\mathbf{r} \to \mathbf{r}_0$ (see details in the Appendix A) one has

$$\nabla\nabla\breve{G}^{\infty}_{\text{spatial}}(\mathbf{r}_0, \mathbf{r}_0, \mathbf{k}_B) = \frac{1}{8\pi}\sum_{n\neq(0,0,0)}e^{i\mathbf{k}_B\cdot\mathbf{d}_n}\underline{\mathbf{F}}_{\text{spatial},n} + \frac{1}{24\pi}\left(f'''(0) + 2ik^3\right)\underline{\mathbf{I}}. \tag{25}$$

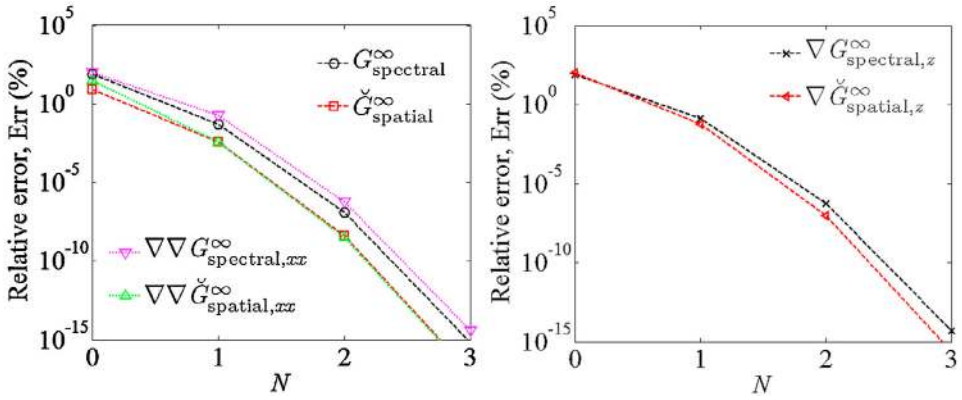

Figure 2. Relative error Err in (31) of the scalar and dyadic quantities in the legends for $\mathbf{k}_B = k_z\hat{\mathbf{z}}$ for the 3D lattice of PbTe microspheres analyzed in section 4 at 25 THz.

3.2. Expressions for the Regularized Antidiagonal Dyad $\breve{\underline{\mathbf{G}}}^{\infty}_{\text{ad}}$

[25] Similarly to what done for the principal diagonal dyad in the previous section, also the dyadic GF in (7) is split into the hybrid sum of spectral and spatial dyadic terms

$$\underline{\mathbf{G}}^{\infty}_{\text{ad}}(\mathbf{r},\mathbf{r}_0,\mathbf{k}_B) = \underline{\mathbf{G}}^{\infty}_{\text{ad,spectral}}(\mathbf{r},\mathbf{r}_0,\mathbf{k}_B) + \underline{\mathbf{G}}^{\infty}_{\text{ad,spectral}}(\mathbf{r},\mathbf{r}_0,\mathbf{k}_B), \quad (26)$$

through the Ewald method, where

$$\underline{\mathbf{G}}^{\infty}_{\text{ad,type}}(\mathbf{r},\mathbf{r}_0,\mathbf{k}_B) = \nabla G^{\infty}_{\text{type}}(\mathbf{r},\mathbf{r}_0,\mathbf{k}_B) \times \underline{\mathbf{I}}, \quad (27)$$

and "type" is either spectral or spatial. The terms $\nabla G^{\infty}_{\text{spectral}}$ and $\nabla G^{\infty}_{\text{spatial}}$ are derived based on (15) and (16) leading to

$$\nabla G^{\infty}_{\text{spectral}}(\mathbf{r},\mathbf{r}_0,\mathbf{k}_B) = \frac{i}{abc}\sum_{n=-\infty}^{+\infty}(\mathbf{k}_B+\mathbf{k}_n)\frac{e^{-\frac{\gamma_n^2}{4E^2}}}{\gamma_n^2}e^{i(\mathbf{k}_B+\mathbf{k}_n)\cdot(\mathbf{r}-\mathbf{r}_0)}, \quad (28)$$

$$\nabla G^{\infty}_{\text{spatial}}(\mathbf{r},\mathbf{r}_0,\mathbf{k}_B) = \frac{1}{8\pi}\sum_{n=-\infty}^{+\infty}e^{i\mathbf{k}_B\cdot\mathbf{d}_n}\left(\frac{f'(R_n)}{R_n}-\frac{f(R_n)}{R_n^2}\right)\hat{\mathbf{R}}_n. \quad (29)$$

[26] Analogously to what discussed for the scalar GF, here $\nabla\breve{G}^{\infty}_{\text{spatial}}(\mathbf{r}_0,\mathbf{r}_0,\mathbf{k}_B) = \lim_{\mathbf{r}\to\mathbf{r}_0}[\nabla G^{\infty}_{\text{spatial}}(\mathbf{r},\mathbf{r}_0,\mathbf{k}_B) - \nabla G(\mathbf{r},\mathbf{r}_0)]$. In its computation we need to evaluate the limit because both $\nabla G^{\infty}_{\text{spatial}}$ and ∇G have singular terms at $\mathbf{r}=\mathbf{r}_0$ of the kind $1/R_0$ and $1/R_0^2$. After performing the limit for $\mathbf{r}\to\mathbf{r}_0$ (see details in Appendix A) one has

$$\nabla\breve{G}^{\infty}_{\text{spatial}}(\mathbf{r}_0,\mathbf{r}_0,\mathbf{k}_B) = \frac{1}{8\pi}\sum_{n\neq(0,0,0)}e^{i\mathbf{k}_B\cdot\mathbf{d}_n}\left(\frac{f'(R_n)}{R_n}-\frac{f(R_n)}{R_n^2}\right)\hat{\mathbf{R}}_n. \quad (30)$$

3.3. Convergence of the Scalar GFs and of the Principal and Antidiagonal Blocks of the Dyadic GF

[27] As stated in section 3.1, the Ewald method allows for obtaining series with Gaussian convergence rate, so only a handful of summation terms are needed to achieve convergence. In order to verify this, we define the relative error as

$$\text{Err}_{\text{spectral}} = \frac{\left|K^N_{\text{spectral}} - K^{\text{exact}}_{\text{spectral}}\right|}{\left|K^{\text{exact}}_{\text{spectral}}\right|} \quad \text{Err}_{\text{spatial}} = \frac{\left|\breve{K}^N_{\text{spatial}} - \breve{K}^{\text{exact}}_{\text{spatial}}\right|}{\left|\breve{K}^{\text{exact}}_{\text{spatial}}\right|} \quad (31)$$

with K_{spectral} either $G^{\infty}_{\text{spectral}}(\mathbf{r}_0,\mathbf{r}_0,\mathbf{k}_B)$, or $\nabla G^{\infty}_{\text{spectral},i}(\mathbf{r}_0,\mathbf{r}_0,\mathbf{k}_B)$, or $\nabla\nabla G^{\infty}_{\text{spectral},ij}(\mathbf{r}_0,\mathbf{r}_0,\mathbf{k}_B)$ and $\breve{K}_{\text{spatial}}$ either $\breve{G}^{\infty}_{\text{spatial}}(\mathbf{r}_0,\mathbf{r}_0,\mathbf{k}_B)$, or $\nabla\breve{G}^{\infty}_{\text{spatial},i}(\mathbf{r}_0,\mathbf{r}_0,\mathbf{k}_B)$, or $\nabla\nabla\breve{G}^{\infty}_{\text{spatial},ij}(\mathbf{r}_0,\mathbf{r}_0,\mathbf{k}_B)$, and $i,j = x,y,z$ indicating the vector and dyad components. In (31), $K^{\text{exact}}_{\text{spectral}}$ and $\breve{K}^{\text{exact}}_{\text{spatial}}$ are evaluated with a sufficiently large number of terms to achieve high numerical accuracy, whereas K^N_{spectral} and $\breve{K}^N_{\text{spatial}}$ are evaluated with $n_1 = n_2 = n_3 = 0, \pm1, \ldots, \pm N$ terms only, as was done in *Capolino et al.* [2005, 2007]. As shown in section 2, the two principal blocks in (12) are proportional to one regularized principal diagonal dyad $\breve{\underline{\mathbf{G}}}^{\infty}_{\text{pd}}$ whereas the two antidiagonal blocks are proportional to one regularized antidiagonal dyad $\breve{\underline{\mathbf{G}}}^{\infty}_{\text{ad}}$. This fact implies that it is sufficient to check the convergence rate of $\breve{\underline{\mathbf{G}}}^{\infty}_{\text{pd}}$ and $\breve{\underline{\mathbf{G}}}^{\infty}_{\text{ad}}$ for a given wave vector $\mathbf{k}_B$.

[28] Consider the 3D lattice of PbTe microspheres shown in Figure 1, and analyzed in section 4, and assume a pseudo-periodic wavefield with frequency of 25 THz. Assume first, for simplicity, a wave vector $\mathbf{k}_B = k_z\hat{\mathbf{z}}$; in Figure 2 we show the relative error Err in (31) of the scalar spectral and spatial GFs in (15) and (19), and of the $\hat{\mathbf{z}}$ (for ∇G^{∞} terms) and the $\hat{\mathbf{x}}\hat{\mathbf{x}}$ (for the $\nabla\nabla G^{\infty}$ terms) components versus the total number of summation terms N computed for their evaluation. Note that for symmetry reasons, it follows that $\nabla G^{\infty}_x = \nabla G^{\infty}_y = 0$, $\nabla\nabla G^{\infty}_{xx} = \nabla\nabla G^{\infty}_{yy} \neq \nabla\nabla G^{\infty}_{zz}$, $\nabla\nabla G^{\infty}_{xy} = \nabla\nabla G^{\infty}_{yx} = 0$, and $\nabla\nabla G^{\infty}_{xz} = \nabla\nabla G^{\infty}_{yz} = \nabla\nabla G^{\infty}_{zx} = \nabla\nabla G^{\infty}_{zy} = 0$.

[29] In general, however, under oblique field propagation also other vector and dyad components play a role. As an example, considering again the 3D lattice of PbTe microspheres analyzed in Figure 1, and in section 4, at 25 THz, and assuming $\mathbf{k}_B = k_B(\sin\theta\hat{\mathbf{x}} + \cos\theta\hat{\mathbf{z}})$ with $\theta = 30°$, we show in Figure 3 the relative error Err in (31) of the $\hat{\mathbf{x}}$ and $\hat{\mathbf{z}}$ (for ∇G^{∞} terms) and the $\hat{\mathbf{x}}\hat{\mathbf{z}}$ and $\hat{\mathbf{z}}\hat{\mathbf{z}}$ (for the $\nabla\nabla G^{\infty}$ terms) components versus the total number of summation terms N computed for their evaluation.

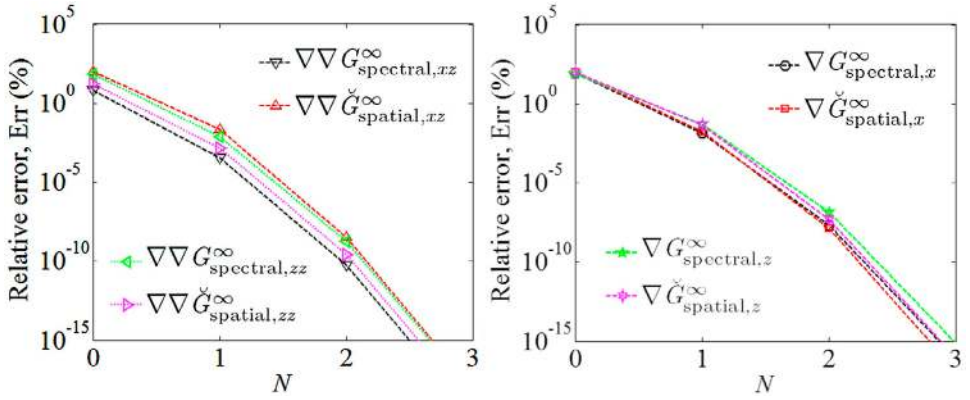

Figure 3. Relative error Err in (31) of the dyadic quantities in the legends for $\mathbf{k}_B = k_B$ (sin $\theta\hat{\mathbf{x}}$ + cos $\theta\hat{\mathbf{z}}$) with $\theta = 30°$ for the 3D lattice of PbTe microspheres analyzed in section 4 at 25 THz.

[30] Note that, as expected, scalar spectral and spatial components in Figures 2 and 3 converge very rapidly, with about the same rate (i.e., same number of summation terms N). The same applies to the shown dyadic quantities. For example, in Figures 2 and 3, Err < 10^{-8} for all the series when using $N = 2$. Note that even $N = 1$ would already guarantee a relative error Err < 10^{-3}.

[31] To provide enough evidence of the functionality of the proposed DDA method, consider the 3D lattice of TiO_2 microspheres shown in Figure 1, and analyzed in section 4, and assume a field is present with frequency of 300 GHz. Assume a wave vector $\mathbf{k}_B = k_z\hat{\mathbf{z}}$; in Figure 4 we show the relative error Err in (31) of the scalar spectral and spatial GFs in (15) and (19), and of the $\hat{\mathbf{z}}$ (for ∇G^{∞} terms) and the $\hat{\mathbf{x}}\hat{\mathbf{x}}$ (for the $\nabla\nabla G^{\infty}$ terms) components versus the total number of summation terms N computed for their evaluation. Similar conclusions to the results in Figure 2 apply to Figure 4.

[32] Last, from a numerical point of view, one can notice that still in the provided numerical examples only a relatively small number of summation terms ($N = 2$) are needed to achieve convergence when using the Ewald method proposed here, with respect to the fully spatial (singular when computed at the dipole location, as in the present case) or the fully spectral (which needs an infinite number of terms to reconstruct the singularity when computed at the dipole location, as in the present case) counterparts.

4. Modes With Real or Complex Wave Number and Description of Composite Materials Through Effective Refractive Index

[33] We analyze some electromagnetic properties of two composite materials made of a 3D array of (i) PbTe microspheres at infrared frequencies and (ii) TiO_2 microspheres at millimeter waves. Due to the high frequency values, one may assume that the chosen material composing the microspheres has $\mu = \mu_0$ (though the effective permeability of the composite μ_{eff} may differ from unity). We compute and compare the modal wave numbers through mode analysis based on three different approximations: (i) single dipole approximation (SDA) using *only electric dipoles* [*Campione et al.*, 2011b], (ii) *only magnetic dipoles* [*Campione et al.*, 2012], and (iii) the DDA that uses both electric and magnetic dipoles discussed in sections 2 and 3 (we assumed $N = 2$ in the evaluation of the GF summations because it already guarantees convergence as explained in the previous section, in the shown frequency range), from which also the effective refractive index is retrieved. We want to stress that the DDA

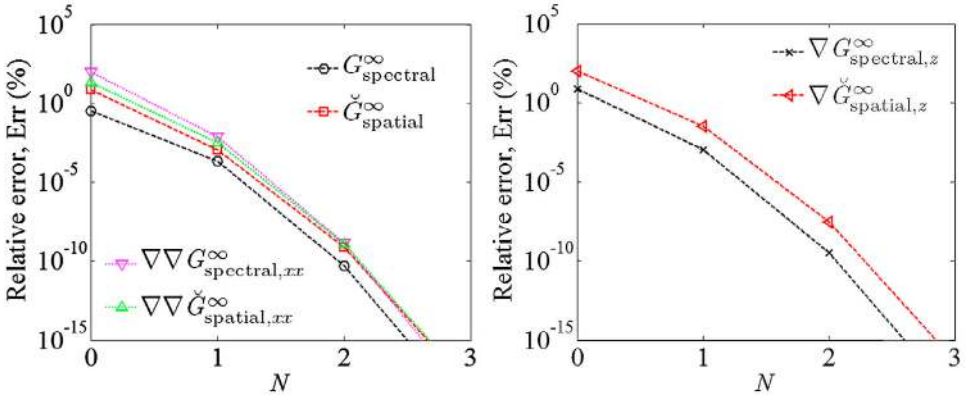

Figure 4. Relative error Err in (31) of the scalar and dyadic quantities in the legends for $\mathbf{k}_B = k_z\hat{\mathbf{z}}$ for the 3D lattice of TiO_2 microspheres analyzed in section 4 at 300 GHz.

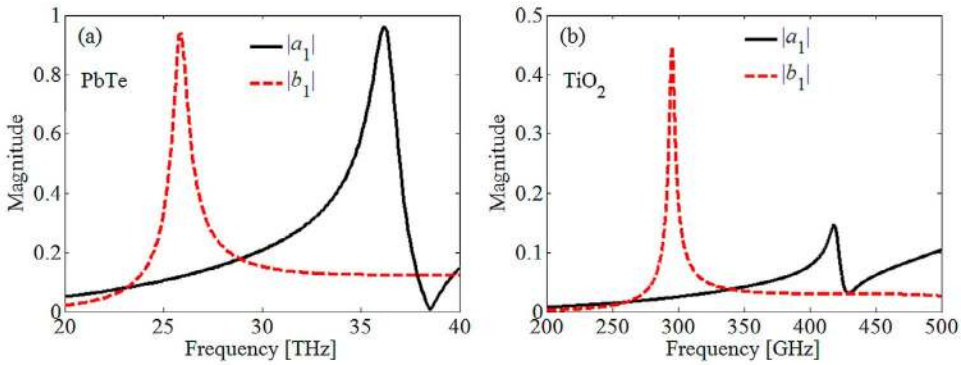

Figure 5. Frequency behavior of the magnitude of the electric (a_1) and magnetic (b_1) Mie dipole coefficients for (a) a PbTe microsphere with radius 1 μm and (b) a TiO_2 microsphere with radius 52 μm.

is a good approximation when the two dipole moments (or any of them) dominate the scattered-field multipole expansion. We also adopt Maxwell Garnett (MG) homogenization theory [*Sihvola*, 1999, 2009], and Nicolson-Ross-Weir (NRW) retrieval method [*Boughriet et al.*, 1997; *Nicolson and Ross*, 1970; *Simovski*, 2009; *Smith et al.*, 2002; *Weir*, 1974] from scattering parameters for finite thickness structures, computed here through a full-wave simulation software employing the finite element method in frequency domain (high frequency structure simulator, HFSS by Ansys Inc.). In general, the NRW solution should be proven to be consistent for varying the number of layers, as shown in *Campione et al.* [2011b] for example. For simplicity in Figures 6–9 we show only the result obtained with 4 layers, because results with other number of layers are found to be in good agreement.

4.1. Microsphere Resonances

[34] We consider microspheres with radius $r = 1$ μm made of PbTe, with permittivity $\varepsilon_m = 32.04 + 0.0524i$ [*Basilio et al.*, 2011; *Palik*, 1985], and with $r = 52$ μm made of TiO_2, with permittivity $\varepsilon_m = \varepsilon'_m + i\varepsilon''_m$, where $\varepsilon'_m = 3.33f + 92.34$ and $\varepsilon''_m = 0.28f^{-2} + 7.64f - 1.54$, with f being the frequency in THz [*Berdel et al.*, 2005; *Lannebere*, 2011]. PbTe microspheres resonate at infrared frequencies between 20 THz and 40 THz, and TiO_2 microspheres resonate at millimeter waves between 200 GHz and 500 GHz. With these assumptions, in Figure 5 we report the magnitude of the Mie dipole-like scattering coefficients a_1 and b_1 (see (10) and (11)) versus frequency. It can be observed that the PbTe (TiO_2) particles, for increasing frequency, exhibit first a magnetic resonance around 26 THz (300 GHz) (due to $|b_1| > |a_1|$) with residual electric contributions, and then an electric resonance around 36 THz (420 GHz) (due to $|a_1| > |b_1|$) with residual magnetic contributions. All these effects are accounted for in the DDA model proposed here, whereas the residual ones are not considered in the SDA models. This is why the DDA solution is expected to provide results in better agreement with the full-wave NRW result than simpler SDA models. Since these two electric and magnetic dipole-like terms are dominant in the scattering process, microsphere electromagnetic interactions can be based only on dipole-dipole mechanisms, including both electric and magnetic kinds.

4.2. Modes With Real or Complex Wave Number

[35] In this section, we first show the modes with real or complex wave number for traveling modes along the z-direction (i.e., $\mathbf{k}_B = k_z\hat{\mathbf{z}}$, with $k_z = \beta_z + i\alpha_z$) with dipole moments polarized along either the x- or y-direction (transversal polarization, "T-pol," with respect to the mode traveling direction) in a 3D periodic array of PbTe microspheres

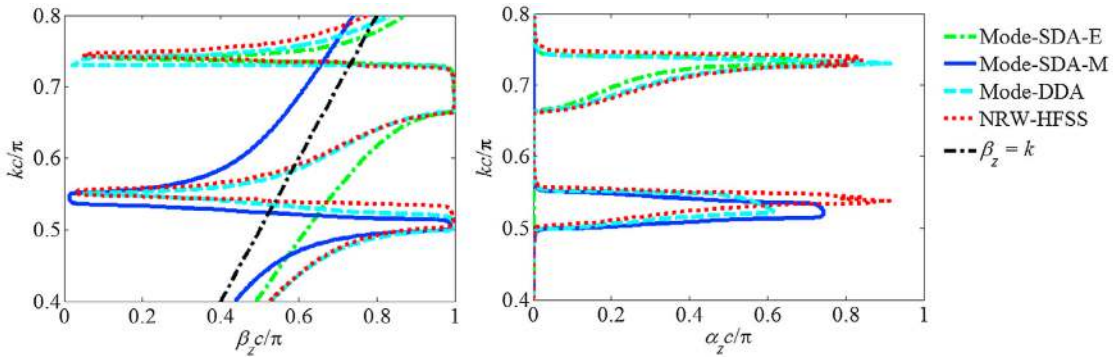

Figure 6. Wave number $k_z = \beta_z + i\alpha_z$ versus normalized frequency dispersion diagram for T-pol modes, for the considered 3D periodic array made of PbTe microspheres, retrieved with four different methods. The DDA is the one that better computes the mode wave number, when compared with NRW-HFSS.

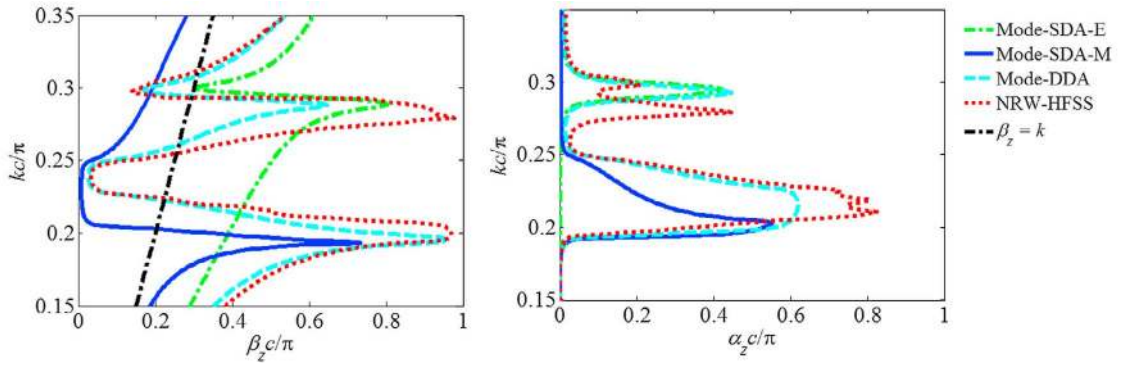

Figure 7. As in Figure 6, for TiO_2 microspheres.

embedded in free space (i.e., $k = k_0$, $\varepsilon_h = 1$) with cubic lattice (i.e., $a = b = c$), with $c = 3$ μm.

[36] The dispersion diagrams for the 3D periodic array described above are shown in Figure 6, computed with various methods: (i) the SDA method (including only magnetic effects Mode-SDA-M, obtained by imposing $\alpha_{ee} = 0$ in (13) and neglecting the contribution from $\underline{\breve{\mathbf{G}}}^{\infty}_{HP}$), (ii) the SDA with only electric effects Mode-SDA-E, obtained by imposing $\alpha_{mm} = 0$ in (13) and neglecting the contribution from $\underline{\breve{\mathbf{G}}}^{\infty}_{EM}$), (iii) the DDA method in (13), and (iv) the NRW method. The latter method is applied as follows: first, reflection and transmission coefficients are retrieved through a HFSS simulation for 4 layers of microspheres. These coefficients are used to retrieve the effective refractive index n_{eff} (see the next section). Then, the modal wave number is retrieved as $k_z = n_{eff} k_0$. The plot in Figure 6 shows only the dominant transverse mode. Other modes with transverse polarization with large attenuation constant α_z, symptom of a weak spatial dispersion, are present and much weaker than the fundamental one. Indeed, the effect of these highly attenuated modes can be neglected as discussed in *Campione et al.* [2011b, 2012]. In Figure 6 one should note how the Mode-SDA-M fails to predict the feature in the range $0.6 < kc/\pi < 0.8$ (i.e., frequency range between 30 and 40 THz), which is mainly related to the strong scattering by the electric dipoles in the same frequency range, shown in Figure 5a. Vice versa, the Mode-SDA-E fails to predict the feature in the range $0.4 < kc/\pi < 0.6$ (i.e., frequency range between 20 and 30 THz), associated to the strong scattering by the magnetic-dipoles in the same frequency range, shown in Figure 5a. On the contrary, the DDA method allows getting results in good agreement with NRW in the entire analyzed frequency range. In this particular case however, the Mode-SDA-M is in good agreement with DDA and NRW in the range $0.45 < kc/\pi < 0.55$ (i.e., frequency range between 22.5 and 27.5 THz, where the magnetic dipole-like scattering is dominant), and the same happens for the SDA-E in the range $0.65 < kc/\pi < 0.8$ (i.e., frequency range between 32.5 and 40 THz, where the electric dipole-like scattering is dominant).

[37] Note however that in general there could be cases where the SDA approximations provide quite different results than the ones computed through NRW in the whole frequency range, as for example shown in *Campione et al.* [2012]. For this reason, we report in Figure 7 the modes with real or complex wave number for traveling modes along the z-direction (i.e., $\mathbf{k}_B = k_z\hat{\mathbf{z}}$, with $k_z = \beta_z + i\alpha_z$) with dipole moments polarized along either the x- or y-direction (transversal polarization, "T-pol," with respect to the mode traveling direction) in a 3D periodic array of TiO_2 microspheres embedded in free space (i.e., $k = k_0$, $\varepsilon_h = 1$) with cubic lattice (i.e., $a = b = c$), with $c = 106$ μm. This case is quite extreme because the spheres are very packed in the lattice (i.e., multipolar terms may have some effect), however the DDA provides results still in good agreement with NRW since it accounts for both electric and magnetic dipolar interactions among microspheres. Note again that the

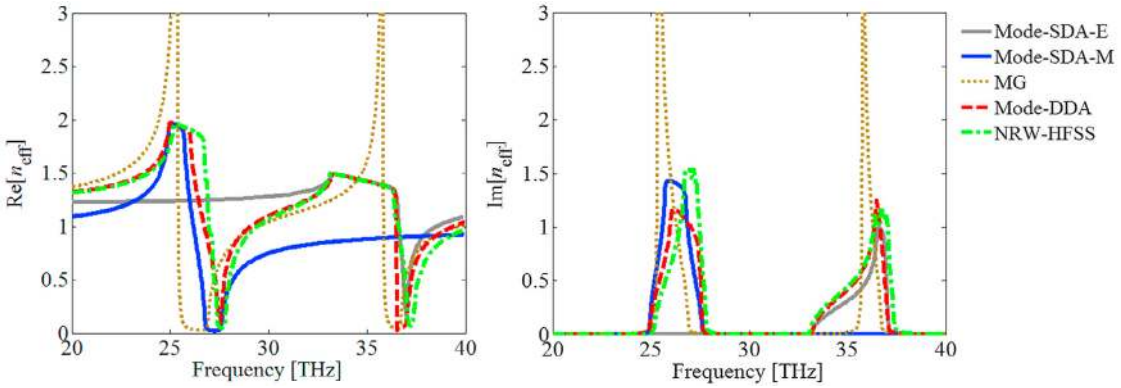

Figure 8. Effective refractive index retrieved by different methods for the array of PbTe microspheres. The DDA method is the one that better computes the refractive index, when compared with the NRW-HFSS. MG is the worst approximation.

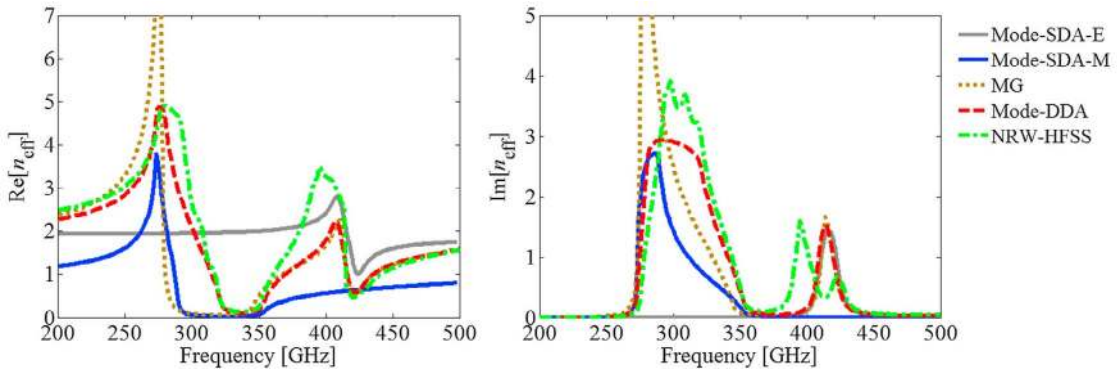

Figure 9. As in Figure 8, for TiO_2 microspheres.

Mode-SDA-M fails to predict the feature in the range $0.25 < kc/\pi < 0.35$ (i.e., frequency range between 350 and 500 GHz), which is mainly related to the strong scattering by the electric dipoles in the same frequency range, shown in Figure 5b. Vice versa, the Mode-SDA-E fails to predict the feature in the range $0.15 < kc/\pi < 0.25$ (i.e., frequency range between 200 and 350 GHz), associated to the strong scattering by the magnetic-dipoles in the same frequency range, shown in Figure 5b. In this case, however, the two SDA models provide curves with only salient propagation features. In contrast, the DDA model allows for a better estimation of the complex propagation constant k_z when compared to the full-wave simulation result (NRW).

4.3. Effective Refractive Index

[38] As described in the previous section one mode only, with transverse polarization, is dominant and able to propagate inside the lattice, and therefore the composite material is now considered for refractive index homogenization. We compute the effective refractive index by using the four methods employed in the previous section, and also by using Maxwell Garnett method [*Sihvola*, 1999, 2009]. In particular, the refractive index can be easily retrieved through modal analysis (SDA or DDA) as $n_{\text{eff}} = k_z/k_0$, with k_z being the complex wave number shown in Figures 6 and 7. With Maxwell Garnett, first ε_{eff} and μ_{eff} are computed independently [*Sihvola*, 1999, 2009], then $n_{\text{eff}} = \sqrt{\varepsilon_{\text{eff}}\mu_{\text{eff}}}$. Through NRW, instead, n_{eff} is computed after retrieving reflection and transmission coefficients through a HFSS simulation with four layers of microspheres. The effective refractive index computed by the five different methods is shown in Figures 8 and 9. Notice how in the considered 3D arrays the DDA method provides a result in very good agreement with the NRW method. Maxwell Garnett is the one that disagrees the most because it does not include field retardation effects and electric-magnetic particle interactions accounted for in all the other methods. Also, in the MG method, electric and magnetic effects are considered separately, and not together as in the DDA or in the NRW methods.

5. Conclusion

[39] A formulation for electromagnetic analysis of composite materials made of periodic arrays of electric and magnetic dipoles has been carried out by using new expressions for the dyadic GF for periodic arrays based on the Ewald method. Then we have used the developed theory to analyze two 3D periodic arrays made of (i) lead telluride (PbTe) and (ii) titanium dioxide (TiO_2) microspheres, for which we have evaluated the modes with real or complex wave number. Each microsphere has been modeled according to the dual (electric and magnetic) dipole approximation (DDA). A mode with transverse polarization has been found to be dominant and able to propagate inside the lattice, thus the composite material has been described through an effective refractive index. Both the modal wave number and homogenized refractive index results have been compared with those obtained from the algorithm based on scattering parameters for finite thicknesses, and from single dipole approximation based on electric or magnetic dipoles only. The effective refractive index has also been calculated from Maxwell Garnett homogenization theory. The proposed DDA method has been found to be in very good agreement with full-wave simulations and showed better performance than the MG and SDA methods.

Appendix A: Regularization of the Spatial Terms of the Dyadic Green's Functions

[40] The regularized GF $\breve{G}^{\infty}_{\text{spatial}}(\mathbf{r}_0, \mathbf{r}_0, \mathbf{k}_B)$ reported in (19) is evaluated by subtracting the $n = (0, 0, 0)$ spherical wave term of the purely spatial GF. This leads to

$$\begin{aligned}\breve{G}^{\infty}_{\text{spatial}}(\mathbf{r}_0,\mathbf{r}_0,\mathbf{k}_B) &= \lim_{\mathbf{r}\to\mathbf{r}_0}\left[G^{\infty}_{\text{spatial}}(\mathbf{r},\mathbf{r}_0,\mathbf{k}_B) - G(\mathbf{r},\mathbf{r}_0)\right] = \\ &= \frac{1}{8\pi}\sum_{n\neq(0,0,0)}\frac{e^{i\mathbf{k}_B\cdot\mathbf{d}_n}}{R_n}f(R_n) \\ &\quad + \lim_{R\to 0}\left[\frac{1}{8\pi}\frac{f(R)}{R} - \frac{1}{4\pi}\frac{e^{ikR}}{R}\right] = \\ &= \frac{1}{8\pi}\sum_{n\neq(0,0,0)}\frac{e^{i\mathbf{k}_B\cdot\mathbf{d}_n}}{R_n}f(R_n) + \frac{f'(0)-2ik}{8\pi} \qquad \text{(A1)}\end{aligned}$$

[41] The same regularization is applied to $\nabla\nabla\breve{\bar{G}}^{\infty}_{\text{spatial}}(\mathbf{r}_0, \mathbf{r}_0, \mathbf{k}_B)$ in (25), which leads to

$$\nabla\nabla\breve{\bar{G}}^{\infty}_{\text{spatial}}(\mathbf{r}_0,\mathbf{r}_0,\mathbf{k}_B) = \lim_{\mathbf{r}\to\mathbf{r}_0}\left[\nabla\nabla G^{\infty}_{\text{spatial}}(\mathbf{r},\mathbf{r}_0,\mathbf{k}_B) - \nabla\nabla G(\mathbf{r},\mathbf{r}_0)\right] = \\ = \frac{1}{8\pi}\sum_{n\neq(0,0,0)} e^{i\mathbf{k}_B\cdot\mathbf{d}_n}\underline{\mathbf{F}}_{\text{spatial},n} + \lim_{\mathbf{R}\to\mathbf{0}}\left[\frac{1}{8\pi}\underline{\mathbf{F}}_{\text{spatial},000} - \nabla\nabla\left(\frac{1}{4\pi}\frac{e^{ikR}}{R}\right)\right] \tag{A2}$$

[42] The limit is evaluated as follows:

$$\lim_{\mathbf{R}\to\mathbf{0}}\left[\frac{1}{8\pi}\underline{\mathbf{F}}_{\text{spatial},000} - \nabla\nabla\left(\frac{1}{4\pi}\frac{e^{ikR}}{R}\right)\right] = \lim_{\mathbf{R}\to\mathbf{0}}\left[\begin{array}{l}\frac{1}{8\pi}\left(\left(\frac{f'(R)}{R^2}-\frac{f(R)}{R^3}\right)\underline{\mathbf{I}} + \left(\frac{f''(R)}{R}-\frac{3f'(R)}{R^2}+\frac{3f(R)}{R^3}\right)\hat{\mathbf{R}}\hat{\mathbf{R}}\right) - \\ \left(\frac{ik}{4\pi}\left(\frac{1}{R^2}-\frac{1}{ikR^3}\right)e^{ikR}\underline{\mathbf{I}} - \frac{2ik}{4\pi}\left(\frac{1}{R^2}-\frac{3}{2ikR^3}\right)e^{ikR}\hat{\mathbf{R}}\hat{\mathbf{R}} - \frac{k^2}{4\pi}\left(\frac{1}{R}-\frac{1}{ikR^2}\right)e^{ikR}\hat{\mathbf{R}}\hat{\mathbf{R}}\right)\end{array}\right] \\ = \frac{1}{24\pi}\left(f'''(0)+2ik^3\right)\underline{\mathbf{I}} \tag{A3}$$

[43] The same regularization is applied to $\nabla\breve{\bar{G}}^{\infty}_{\text{spatial}}(\mathbf{r}_0, \mathbf{r}_0, \mathbf{k}_B)$ in (30), which leads to

$$\nabla\breve{\bar{G}}^{\infty}_{\text{spatial}}(\mathbf{r}_0,\mathbf{r}_0,\mathbf{k}_B) = \lim_{\mathbf{r}\to\mathbf{r}_0}\left[\nabla G^{\infty}_{\text{spatial}}(\mathbf{r},\mathbf{r}_0,\mathbf{k}_B) - \nabla G(\mathbf{r},\mathbf{r}_0)\right] = \\ = \frac{1}{8\pi}\sum_{n\neq(0,0,0)} e^{i\mathbf{k}_B\cdot\mathbf{d}_n}\left(\frac{f'(R_n)}{R_n}-\frac{f(R_n)}{R_n^2}\right)\hat{\mathbf{R}}_n + \lim_{\mathbf{R}\to\mathbf{0}}\left[\frac{1}{8\pi}\left(\frac{f'(R)}{R}-\frac{f(R)}{R^2}\right)\hat{\mathbf{R}} - \nabla\left(\frac{1}{4\pi}\frac{e^{ikR}}{R}\right)\right] \tag{A4}$$

[44] The limit is evaluated as follows:

$$\lim_{\mathbf{R}\to\mathbf{0}}\left[\frac{1}{8\pi}\left(\frac{f'(R)}{R}-\frac{f(R)}{R^2}\right)\hat{\mathbf{R}} - \nabla\left(\frac{1}{4\pi}\frac{e^{ikR}}{R}\right)\right] = \\ = \lim_{\mathbf{R}\to\mathbf{0}}\left[\frac{1}{8\pi}\left(\frac{f'(R)}{R}-\frac{f(R)}{R^2}\right)\hat{\mathbf{R}} - \frac{1}{4\pi}\left(\frac{ike^{ikR}}{R}-\frac{e^{ikR}}{R^2}\right)\hat{\mathbf{R}}\right] = \\ = \lim_{\mathbf{R}\to\mathbf{0}}\left[\frac{1}{16\pi}\left(f''(R)+2k^2e^{ikR}\right)\hat{\mathbf{R}}\right] = \mathbf{0} \tag{A5}$$

Appendix B: Supporting Mathematical Expressions

[45] The expressions for the derivatives of the function f in (17) are here summarized. The first derivative f' (with respect to the argument R_n) is given by

$$f'(R_n) = ik\left[e^{+ikR_n}\text{erfc}\left(\beta^+\right) - e^{-ikR_n}\text{erfc}\left(\beta^-\right)\right] - (A+B), \tag{B1}$$

where

$$A = \frac{2E}{\sqrt{\pi}}e^{-(\beta^-)^2}e^{-ikR_n}, \quad B = \frac{2E}{\sqrt{\pi}}e^{-\left(\beta^+\right)^2}e^{ikR_n}. \tag{B2}$$

[46] The second derivative f'' is given by

$$f''(R_n) = -k^2 f(R_n) + 2ik(A-B) + (C+D), \tag{B3}$$

where

$$C = \frac{4E^2}{\sqrt{\pi}}\beta^- e^{-(\beta^-)^2}e^{-ikR_n}, \quad D = \frac{4E^2}{\sqrt{\pi}}\beta^+ e^{-\left(\beta^+\right)^2}e^{ikR_n}. \tag{B4}$$

[47] The third derivative f''' is given by

$$f'''(R_n) = -k^2 f'(R_n) + 3ik(D-C) + \left(2k^2+2E^2\right)(A+B) + \\ - \frac{8E^3}{\sqrt{\pi}}\left[(\beta^-)^2 e^{-(\beta^-)^2}e^{-ikR_n} + \left(\beta^+\right)^2 e^{-\left(\beta^+\right)^2}e^{ikR_n}\right]. \tag{B5}$$

[48] Last, note that (17), (B1), (B3) and (B5), when computed for $R_n = 0$ as required in (A1), (A3) and (A5), assume the following values:

$$f(0) = 2, \quad f'(0) = -\frac{4E}{\sqrt{\pi}}e^{\frac{k^2}{4E^2}} + ik\left[\text{erfc}\left(\frac{ik}{2E}\right) - \text{erfc}\left(-\frac{ik}{2E}\right)\right], \\ f''(0) = -2k^2, \quad f'''(0) = \frac{8E^3}{\sqrt{\pi}}e^{\frac{k^2}{4E^2}} - k^2 f'(0). \tag{B6}$$

[49] **Acknowledgments.** We acknowledge partial support from the National Science Foundation, award NSF-CMMI 1101074. The authors also thank Ansys Inc. for providing HFSS that was instrumental in this analysis. We also acknowledge useful discussions with R. Shore and A. Yaghjian, originally with Air Force Research Laboratory, Hanscom AFB, Massachusetts, and with M. Albani from the University of Siena, Italy.

References

Abramowitz, M., and I. A. Stegun (1965), *Handbook of Mathematical Functions with Formulas, Graphs, and Mathematical Tables*, Dover, New York.

Alù, A., and N. Engheta (2006), Erratum: "Polarizabilities and effective parameters for collections of spherical nanoparticles formed by pairs of concentric double-negative, single-negative, and/or double-positive metamaterial layers" [J. Appl. Phys. 97, 094310 (2005)], *J. Appl. Phys.*, *99*(6), 069901, doi:10.1063/1.2185829.

Alù, A., and N. Engheta (2007), Three-dimensional nanotransmission lines at optical frequencies: A recipe for broadband negative-refraction optical metamaterials, *Phys. Rev. B*, *75*(2), 024304, doi:10.1103/PhysRevB.75.024304.

Basilio, L. I., L. K. Warne, W. L. Langston, W. A. Johnson, and M. B. Sinclair (2011), A negative-index metamaterial design based on metal-core, dielectric shell resonators, paper presented at 2011 IEEE International Symposium on Antennas and Propagation (APSURSI), IEEE, Spokane, Wash., 3–8 July.

Benenson, L. S. (1971), Dispersion equations of periodic structures, *Radio Eng. Electron. Phys. Engl. Transl.*, *16*(8), 1280–1290.

Berdel, K., J. G. Rivas, P. H. Bolivar, P. de Maagt, and H. Kurz (2005), Temperature dependence of the permittivity and loss tangent of high-

permittivity materials at terahertz frequencies, *IEEE Trans. Microwave Theory Tech.*, *53*(4), 1266–1271, doi:10.1109/TMTT.2005.845752.

Bohren, C. F., and D. R. Huffman (1983), *Absorption and Scattering of Light by Small Particles*, John Wiley, New York.

Boughriet, A. H., C. Legrand, and A. Chapoton (1997), Noniterative stable transmission/reflection method for low-loss material complex permittivity determination, *IEEE Trans. Microwave Theory Tech.*, *45*(1), 52–57, doi:10.1109/22.552032.

Campione, S., M. Albani, and F. Capolino (2011a), Complex modes and near-zero permittivity in 3D arrays of plasmonic nanoshells: Loss compensation using gain, *Opt. Mater. Express*, *1*(6), 1077–1089, doi:10.1364/OME.1.001077.

Campione, S., S. Steshenko, M. Albani, and F. Capolino (2011b), Complex modes and effective refractive index in 3D periodic arrays of plasmonic nanospheres, *Opt. Express*, *19*(27), 26,027–26,043, doi:10.1364/OE.19.026027.

Campione, S., S. Lannebère, A. Aradian, M. Albani, and F. Capolino (2012), Complex modes and artificial magnetism in three-dimensional periodic arrays of titanium dioxide microspheres at millimeter waves, *J. Opt. Soc. Am. B Opt. Phys.*, *29*(7), 1697–1706, doi:10.1364/JOSAB.29.001697.

Capolino, F. (Ed.) (2009), *Metamaterials Handbook*, CRC Press, Boca Raton, Fla.

Capolino, F., D. R. Wilton, and W. A. Johnson (2005), Efficient computation of the 2-D Green's function for 1-D periodic structures using the Ewald method, *IEEE Trans. Antennas Propag.*, *53*(9), 2977–2984, doi:10.1109/TAP.2005.854556.

Capolino, F., D. R. Wilton, and W. A. Johnson (2007), Efficient computation of the 3D Green's function for the Helmholtz operator for a linear array of point sources using the Ewald method, *J. Comput. Phys.*, *223*(1), 250–261, doi:10.1016/j.jcp.2006.09.013.

Collin, R. E. (1960), *Field Theory of Guided Waves*, McGraw Hill, New York.

Ewald, P. P. (1921), The calculation of optical and electrostatic grid potential, *Ann. Phys.*, *64*(3), 253–287.

Ham, F. S., and B. Segall (1961), Energy bands in periodic lattices - Green's function method, *Phys. Rev.*, *124*(6), 1786–1796, doi:10.1103/PhysRev.124.1786.

Ishimaru, A., L. Seung-Woo, Y. Kuga, and V. Jandhyala (2003), Generalized constitutive relations for metamaterials based on the quasi-static Lorentz theory, *IEEE Trans. Antennas Propag.*, *51*(10), 2550–2557, doi:10.1109/TAP.2003.817565.

Kustepeli, A., and A. Q. Martin (2000), On the splitting parameter in the Ewald method, *IEEE Microw. Guided Wave Lett.*, *10*(5), 168–170, doi:10.1109/75.850366.

Lannebere, S. (2011), Étude théorique de métamatériaux formés de particules diélectriques résonantes dans la gamme submillimétrique: Magnétisme artificiel et indice de réfraction négatif, PhD thesis, Univ. Bordeaux 1, Bordeaux, France.

Lovat, G., P. Burghignoli, and R. Araneo (2008), Efficient evaluation of the 3-D periodic Green's function through the Ewald method, *IEEE Trans. Microwave Theory Tech.*, *56*(9), 2069–2075, doi:10.1109/TMTT.2008.2002232.

Mulholland, G. W., C. F. Bohren, and K. A. Fuller (1994), Light scattering by agglomerates - Coupled electric and magnetic dipole method, *Langmuir*, *10*(8), 2533–2546, doi:10.1021/la00020a009.

Nicolson, A. M., and G. F. Ross (1970), Measurement of the intrinsic properties of materials by time-domain techniques, *IEEE Trans. Instrum. Meas.*, *19*(4), 377–382, doi:10.1109/TIM.1970.4313932.

Palik, E. (1985), *Handbook of Optical Constants of Solids*, Academic, San Diego, Calif.

Park, M.-J., J. Park, and S. Nam (1998), Efficient calculation of the Green's function for the rectangular cavity, *IEEE Microw. Guided Wave Lett.*, *8*(3), 124–126, doi:10.1109/75.661136.

Shore, R. A., and A. D. Yaghjian (2007), Traveling waves on two- and three-dimensional periodic arrays of lossless scatterers, *Radio Sci.*, *42*, RS6S21, doi:10.1029/2007RS003647.

Shore, R. A., and A. D. Yaghjian (2010), Complex waves on 1D, 2D, and 3D periodic arrays of lossy and lossless magnetodielectric spheres, *Rep. AFRL-RY-HS-TR-2010-0019*, Air Force Res. Lab., Hanscom AFB, Mass.

Shore, R., and A. D. Yaghjian (2012), Complex waves on periodic arrays of lossy and lossless permeable spheres. Part 1: Theory, *Radio Sci.*, *47*, RS2014, doi:10.1029/2011RS004859.

Sihvola, A. (1999), *Electromagnetic Mixing Formulas and Applications*, IET Publ., London, doi:10.1049/PBEW047E.

Sihvola, A. (2009), Mixing rules, in *Theory and Phenomena of Metamaterials*, edited by F. Capolino, chap. 9, CRC Press, Boca Raton, Fla., doi:10.1201/9781420054262.ch9.

Simovski, C. R. (2009), On the extraction of local material parameters of metamaterials from experimental or simulated data, in *Theory and Phenomena of Metamaterials*, edited by F. Capolino, chap. 11, CRC Press, Boca Raton, Fla., doi:10.1201/9781420054262.ch11.

Smith, D. R., S. Schultz, P. Markoscaron, and C. M. Soukoulis (2002), Determination of effective permittivity and permeability of metamaterials from reflection and transmission coefficients, *Phys. Rev. B*, *65*(19), 195104, doi:10.1103/PhysRevB.65.195104.

Steshenko, S., and F. Capolino (2009), Single dipole approximation for modeling collections of nanoscatterers, in *Theory and Phenomena of Metamaterials*, edited by F. Capolino, chap. 8, CRC Press, Boca Raton, Fla., doi:10.1201/9781420054262.ch8.

Stevanoviæ, I., and J. R. Mosig (2007), Periodic Green's function for skewed 3-D lattices using the Ewald transformation, *Microwave Opt. Technol. Lett.*, *49*(6), 1353–1357, doi:10.1002/mop.22429.

Weir, W. B. (1974), Automatic measurement of complex dielectric constant and permeability at microwave frequencies, *Proc. IEEE*, *62*(1), 33–36, doi:10.1109/PROC.1974.9382.

Wheeler, M. S., J. S. Aitchison, and M. Mojahedi (2005a), Magnetism and effective electromagnetic parameters from dielectric spheres, paper presented at Second IASTED International Conference on Antennas, Radar, and Wave Propagation, Int. Assoc. of Sci. and Technol. for Dev., Banff, Alberta, Canada, 9–21 July.

Wheeler, M. S., J. S. Aitchison, and M. Mojahedi (2005b), Three-dimensional array of dielectric spheres with an isotropic negative permeability at infrared frequencies, *Phys. Rev. B*, *72*(19), 193103, doi:10.1103/PhysRevB.72.193103.

Yaghjian, A. D. (1980), Electric dyadic Green's functions in the source region, *Proc. IEEE*, *68*(2), 248–263, doi:10.1109/PROC.1980.11620.